

In situ neutron radiography analysis of graphite/NCA lithium-ion battery during overcharge

Adam Same · Vincent Battaglia · Hong-Yue Tang ·
Jae Wan Park

Received: 19 July 2011 / Accepted: 17 October 2011 / Published online: 19 November 2011
© Springer Science+Business Media B.V. 2011

Abstract Overcharge of lithium-ion batteries can lead to the deposition of lithium ions on the surface of graphite electrodes. The phenomenon of lithium deposition causes reduced electrochemical performance and presents safety concerns for lithium-ion batteries in high-power applications. This study presents a technique using neutron radiography (NR) for in situ visualization of the effects of overcharge in a graphite/NCA ($\text{LiNi}_{0.8}\text{Co}_{0.15}\text{Al}_{0.05}\text{O}_2$) lithium-ion cell. Patterns of deposition of solid material on the surface of the graphite electrode observed in the radiographs were confirmed by direct observation of the electrode. Inductively coupled plasma mass spectrometry was used to verify the elemental contents of the deposited material. NR is shown to be a promising tool for the study of lithium-ion batteries in high-power applications.

Keywords Neutron radiography · Lithium-ion battery · Lithium deposition

Abbreviations

DC	Direct current
DEC	Diethyl carbonate
EC	Ethylene carbonate
mAh	Milliamphour
MCMB	Meso carbon microbead
MNRC	McClellan Nuclear Research Center

<i>n</i>	Neutrons
NCA	$\text{LiNi}_{0.8}\text{Co}_{0.15}\text{Al}_{0.05}\text{O}_2$
NR	Neutron radiography
OCV	Open-circuit voltage
PVDF	Polyvinylidene difluoride
TRIGA	Training, Research, Isotope Production and General Atomic

1 Introduction

Lithium-ion batteries are a preferred energy storage technology for mobile and transportation applications due to their superior energy and power density compared to other battery chemistries [1]. The lithium-ion technology was patented in the 1980s and commercialized in the early 1990s. Since then, advanced materials such as graphite intercalation compounds have improved the safety of the high-energy lithium-ion cell [2]. However, safety concerns and limited life span are still significant challenges of using lithium-based batteries in high-power applications [3–5]. Overcharge of batteries is a particular concern. Charging a cell at high power may cause the voltage of the cell to exceed the maximum value for safe operation. Overcharge is possible even in the presence of charging protection circuitry or battery management systems because active protection systems are not immune to malfunction.

Detrimental effects during overcharge include gas evolution from liquid electrolytes and thermal runaway of the battery [6–8]. Another significant problem is the deposition of lithium onto the surface of the negative electrode. The operation of a lithium-ion cell is governed by electrochemical reactions involving insertion and extraction of lithium ions (Li^+). Upon charging, Li^+ ions are extracted

A. Same · H.-Y. Tang · J. W. Park (✉)
Department of Mechanical and Aeronautical Engineering,
University of California, Davis, 1 Shields Avenue,
Davis, CA 95616, USA
e-mail: jwpark@ucdavis.edu

V. Battaglia
Lawrence Berkeley National Laboratory, 1 Cyclotron Road,
Berkeley, CA 94720, USA

from the positive electrode (cathode) and inserted into specific sites within the structure of the negative electrode (anode) material [9]. When a cell is overcharged, the available insertion sites in the anode become saturated with Li^+ ions, and the ability of additional ions to insert into the electrode material is reduced. An overcharged cell typically results in a rapid rise in the positive electrode potential as all of the Li^+ ions are removed and subsequent deposition of Li on the anode [10]. The deposited lithium may in turn react with the electrolyte to form a solid deposit of lithium carbonate (Li_2CO_3) that can accumulate on the electrode surface. This mechanism was investigated experimentally by Saito et al. [11] for cells with NCA ($\text{LiNi}_{0.8}\text{Co}_{0.15}\text{Al}_{0.05}\text{O}_2$) cathodes.

Lithium deposition and Li_2CO_3 formation both result in severely adverse and irreversible effects on the performance and safety of a Li-ion battery. Solid lithium deposited on a cell electrode may propagate in dendrite- or fiber-like shapes, which can penetrate the separator and cause an internal short circuit in the cell [1, 12]. Internal shorts are often accompanied by rapid heat generation, fire, and/or explosion [1]. The issue of safety presents challenges to the use of lithium-ion batteries in high-power applications such as electric-drive vehicles.

The phenomenon of lithium deposition has been discussed in the literature using both experimental and analytical means. Models developed by Chazalviel and Rosso et al. show that electrochemical deposition is driven by the presence of a strong electric field in the vicinity of the electrode [13, 14]. These models are supported experimentally by Brissot et al. [15, 16], who describe a technique that allows direct in situ observation of dendritic growth in experimental lithium polymer cells. They observe lithium deposition at both high and low current density; the dendrites observed in their work are on the order of 300–400 μm in length. Arora et al. [17] developed an analytical model to simulate the lithium deposition reaction and Li_2CO_3 formation. It is shown in their work that the formation of insoluble Li_2CO_3 on the electrodes is related to higher internal cell resistance and capacity loss. Rosso et al. [18] later expanded the experimental literature on deposition in lithium polymer cells. They utilized scanning electron microscopy to demonstrate that dendritic structures could short-circuit a cell and produce a fuse effect with the passing of current. Santhanagopalan et al. [19] further studied the internal short-circuit behavior of lithium-ion cells, presenting a correlation between the temperature rise in a short-circuited cell and the degree of lithiation of the anode. Thus, a cell with deposits of lithium on the negative electrode is more prone to excessive heating and thermal runaway due to the possible reaction of lithium metal with electrolyte solvents and other cell components.

Tang et al. [20] modeled the distribution of lithium deposition along the profile of a negative electrode. Their work states that lithium deposition is more likely to occur at the edges of the electrode, as the accessibility of the electrode to the electrochemical reaction is greater at the edge than in the center. In order to reduce the occurrence of lithium deposition, they explain that the negative electrode of a cell is typically constructed with a larger area than the positive electrode. Local deposition of lithium may occur even in situations where the average conditions across the electrode are not favorable for this reaction.

There is a need for a technique of analyzing and measuring the deposition of solid material on electrode surfaces within lithium-ion cells to facilitate the development and optimization of battery materials and systems for electric-drive vehicles. To this point, the literature does not include much work that involves visualization of lithium deposition around the profile of an entire electrode. This study demonstrates the applicability of neutron radiography (NR) as a practical tool for the nondestructive inspection of lithium deposition and solid deposit formation in lithium-ion batteries. The ultimate objective of this research is to apply NR to the study of batteries for vehicles with electric-drive trains. Herein, we present some initial results from fundamental experimentation conducted at the University of California, Davis. The following section introduces the theory behind NR and the relevance of this technique to the study of electrochemical cells.

2 Strategy

2.1 Application of neutron radiography to the analysis of lithium-ion batteries

Nondestructive methods of inspection and visualization are desirable for the study of electrochemical cells. In particular, nondestructive, in situ analysis may enable better understanding of mass transfer mechanisms within modern energy storage devices. NR is a useful technique that allows generation of a visual image based on the attenuation or penetration of neutrons through an object of interest [21]. When an object is exposed to a beam of neutrons, the nuclei of the atoms making up the object interact with the beam of neutrons. Different elements absorb and scatter neutrons based on their neutron cross-section. Neutrons that are transmitted through the object impinge on a scintillator screen, which ejects photons for each detected neutron. A charged coupled device (CCD) camera captures an image of the light generated by the scintillator. A two-dimensional radiograph image of the object is generated by the camera in which the intensity of light is correlated to

the object's local elemental composition by the Lambert–Beer attenuation law, described in Eq. 1 [22].

Lambert–Beer attenuation law [22]

$$\varphi = \varphi_0 \exp(-\Sigma * t) \quad (1)$$

The transmitted neutron intensity (φ) through an object is a function of the incident neutron intensity (φ_0), and the product of the macroscopic neutron cross-section of the material (Σ) and the material thickness (t). Changes in local intensity over a series of in situ images can therefore be attributed to mass transfer within the cell.

Neutron imaging has been demonstrated in industrial applications for the examination of fluid ingress and corrosion in aircraft components [23], for the inspection of o-rings in flight-critical aviation systems [24], and for the visualization of oil and sediments within steel pipes [25]. In addition to these uses, the study of lithium-ion batteries is a particularly strong candidate for application of NR. The visualization capability of NR is beneficial for the study and design of advanced batteries for applications in the transportation, medical, and military fields. Goers et al. [26] demonstrate the ability to study gas evolution in an experimental cell using neutron imaging techniques. Lanz et al. [27] provide another study using radiography to visualize changes in liquid electrolyte levels within a commercial lithium-ion cell. In situ visualization of mass transport inside electrochemical cells is a valuable method of understanding the properties of electrode and electrolyte materials.

The Green Transportation Laboratory at the University of California-Davis aims to apply NR to the study of solid deposition on electrodes in lithium-ion batteries. Lithium deposition is one particular occurrence that can be visualized using neutron imaging. The neutron attenuation cross-section of lithium is greater than other materials commonly found in advanced batteries [28]. Radiograph images are therefore able to show high contrast between lithium and other surrounding materials in an electrochemical cell. The ability to visualize the movement and accumulation of lithium ions has been demonstrated in literature [29]. Interest now turns to using this technique to study the detrimental effects of overcharging a lithium-ion battery.

2.2 Experimental setup

A coin-shaped lithium-ion cell was prepared by the Advanced Energy Technologies Department at the Lawrence Berkeley National Laboratory. The cell was constructed with an NCA cathode (LiNi_{0.8}Co_{0.15}Al_{0.05}O₂; 87.2 wt% NCA; 8 wt% PVDF; 4.8 wt% Acetylene Black) and a MCMB graphite anode (88.8 wt% MCMB; 8 wt% PVDF; 3.2 wt% Acetylene Black) inside a thin cylindrical (coin-shaped) stainless steel case. The liquid electrolyte

was 1 mol/L LiPF₆ in EC/DEC (1:1 weight ratio) solvent. The diameter of the cell was 23 mm (0.90 in.), and the thickness was 2 mm (0.08 in.). The mass of the cell was approximately 3 g. The cell had a nominal energy storage capacity of 2.5 mAh. The design minimum operating voltage of the cell was 3.0 V, and the design maximum voltage was 4.1 V. Tests were carried out at room temperature, approximately 25 °C.

The cell was fixed between two overlapping aluminum plates, each 125 mm long by 50 mm wide and 5 mm thick. The aluminum fixture was used to hold the cell in place during experimentation. One cable was attached to each plate using a nut and bolt, and thus, the aluminum plates also provided positive and negative contacts for charging. Battery charging was accomplished using a DC power supply (Acopian Y08LX6400 series) with a custom control program written in LabVIEW 2009. A National Instruments data acquisition (DAQ) system (USB-6008 series) provided the interface between the power supply and the control software.

Testing was carried out at the UC Davis McClellan Nuclear Research Center (MNRC) in North Highlands, CA. The facility features a 2-megawatt Training, Research, Isotope Production and General Atomic (TRIGA) reactor. MNRC features three neutron imaging bays. This experiment was carried out in MNRC Bay 3, shown in Fig. 1. The average neutron beam intensity in this bay is 10⁷ n/cm²s. The length-to-diameter ratio of the neutron beam is 140, which yields a spatial image resolution in radiograph images of approximately 0.1 mm. The aluminum charging fixture was mounted directly on the scintillator screen inside the bay. As the electrodes of the experimental cell were less than 0.1 mm in thickness, neutron imaging was carried out in the direction perpendicular to the plane of the cell electrodes. Constructing the fixture out of aluminum was advantageous because aluminum has a very low attenuation coefficient for thermal neutrons and thus creates a very small amount of interference with the radiograph image.

The open-circuit voltage (OCV) of the cell was measured to be 3.7 V prior to the experiment. An experimental power profile was designed to apply a constant DC voltage in order to charge the cell to a voltage greater than the design maximum value of 4.1 V. Charging was done in two separate stages. The cell was first charged using a constant voltage of 4.5 V for 20 min. The cell was then charged using a constant voltage of 4.8 V for 40 min. Cell voltage was monitored in situ using a digital multimeter. The experimental voltage profile is shown in Fig. 2.

Two calibration radiographs were taken prior to experimentation. A dark field image (with no incident radiation) and a flat field image (with full incident radiation but no

Fig. 1 Neutron radiography imaging setup in MNRC Bay 3 [30]. *Inset* shows aluminum charging fixture used for this study. The cell is fixed between two individual plates. A pocket of material was removed from each plate to reduce the thickness of aluminum around the cell and produce a better radiograph image

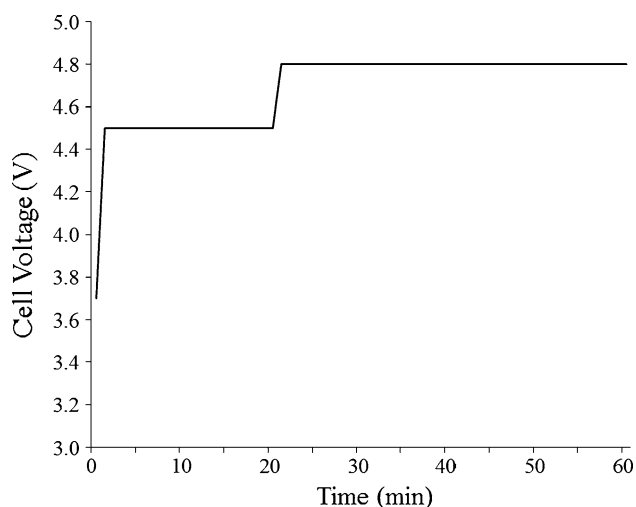
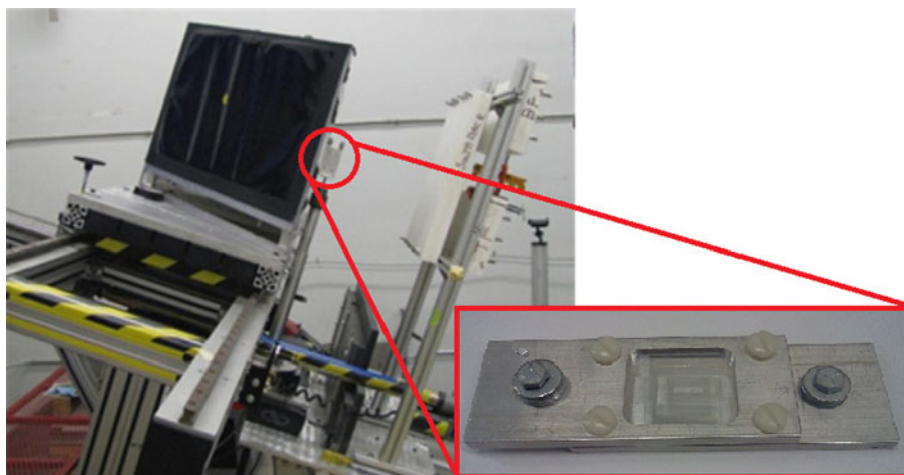


Fig. 2 Experimental charging profile for overcharge test

object in the beam path) were used to determine the background intensity of the neutron beam. Preliminary radiograph images were then taken of the cell and fixture to determine the exposure time and frame averaging required to achieve good image quality. Longer exposure times result in better contrast between materials shown in the image, but temporal resolution of the experiment is lost at very long exposures. Frame averaging involves combining the attenuation maps of several radiographs. This practice allows the reduction of noise in the image, as sharp anomalies in intensity between the images can be eliminated when averaged together. However, averaging extra frames in each image creates a similar challenge to temporal resolution. An exposure time of 45 s was selected for this study. Noise was found to be sufficiently reduced by averaging two frames per image. These parameters allowed collection of one radiograph image every 2 min. A total of

30 radiograph images were generated throughout the 60-min test.

2.3 Image processing

Radiograph images from this experiment were processed in order to isolate the differences in neutron attenuation between the in situ radiographs and a pretest image. Data files for each radiograph were imported into the Imgrex program and converted to bitmap format. The resolution of the resulting bitmap images was $2,048 \times 2,048$ pixels. Data points that registered as pure white or pure black pixels were regarded as noise due to a clear lack of continuity with the surrounding pixels in the image. The clarity of the bitmap files was enhanced by performing a despeckle operation in ImageJ. This process improved the quality of the images by replacing the aforementioned noisy data points with values that were closer to the local average. The bitmap images were then imported into MATLAB. Each pixel in a bitmap file is represented in MATLAB by a numerical value between 0 (pure black) and 255 (pure white), with the data stored in matrix form. The pixel data values for each radiograph were divided by the corresponding pixels in the pretest data. The logarithm of this quotient is proportional to the difference in material thickness, as shown in Eq. 2.

Application of Lambert–Beer Law to change in material thickness

$$\ln(\phi_2/\phi_1) = \sum * (t_1 - t_2) \quad (2)$$

Color maps were applied in MATLAB to convert grayscale images to color, highlighting the regions of the cell with the most pronounced variations in neutron attenuation. The following section presents the results of radiography and image processing.

3 Results

3.1 Pretest radiography

Preliminary imaging confirmed the ability of the neutron beam in MNRC Bay 3 to penetrate through the aluminum fixture and the stainless steel battery case. A pretest radiograph image of the coin cell and fixture is shown in Fig. 3. The low attenuation of aluminum results in the fixture plates being faintly distinguishable from the background of the image. The two bolts with cables attached for

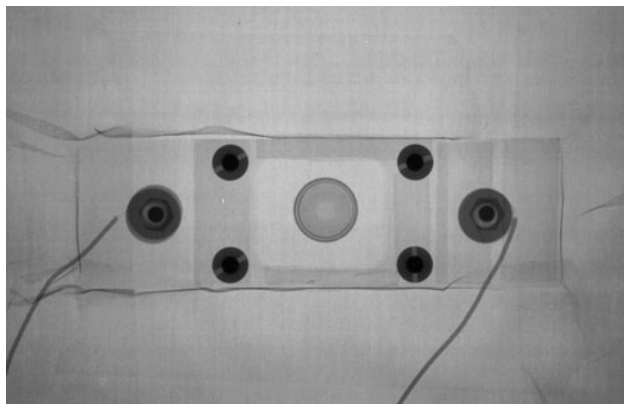


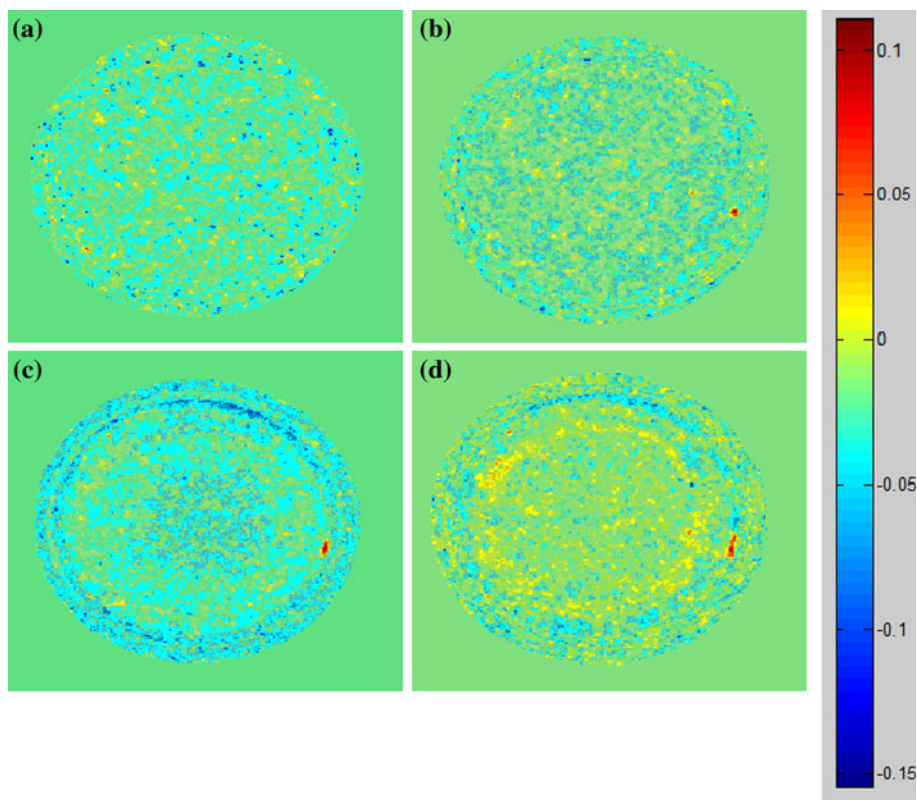
Fig. 3 In situ radiograph image of coin cell and fixture. The cell is visible in the center of the fixture

the positive and negative connections are visible in a darker intensity due to the greater attenuation of neutrons by the carbon steel in the bolts. Similarly, the four nylon bolts securing the fixture plates together show up as dark in the image. The coin cell is shown in the center of the fixture. Some details of the cell are clearly visible, including the seal around the edge of the case and the cell spring in the center. The profile of the cell electrodes is faintly visible. Preliminary radiography thus verified the ability of the neutron beam to penetrate the battery and generate a useful image of the cell internals.

3.2 In situ radiography

Results from Lambert–Beer image division and post-processing are shown in Fig. 4. A color map was applied to the images using MATLAB to qualitatively highlight variations in neutron intensity. Regions of little to no change between images are shown as blue or green on the color map; the negligible change in neutron intensity is attributed to background variations in neutron flux within the radiography bay. Areas of greater local change in neutron attenuation are colored orange or red. Figure 4a shows the cell 2 min after the start of the test; the division of the 2-min radiograph against the pretest image predictably shows no change in the cell. Figure 4b shows the cell after being subjected to a charging voltage of 4.5 V for 20 min.

Fig. 4 Processed radiograph images of NCA coin cell: **a** 2 min into test; cell voltage = 4.5 V; **b** 20 min into test; cell voltage = 4.5 V; **c** 32 min into test; cell voltage = 4.8 V; **d** 40 min into test; cell voltage = 4.8 V. A color scale is provided for qualitative comparison; higher values (red color/darker grayscale) indicate greater change in neutron attenuation compared to the pre-test radiograph. (Color figure online)



A region of higher local neutron attenuation can be seen developing on the right side of the coin cell. This region increases in size as the charging voltage is increased to 4.8 V. Figure 4c shows the cell 32 min into the test. A faint ring of increased attenuation is developing around the center of the cell. This trend propagates as the cell voltage is held at 4.8 V. After 40 min of charging, as seen in Fig. 4d, neutron attenuation around the profile of the cell electrodes continues to increase.

Figure 5a shows the cell after 60 min of overcharging, at the end of the test. High neutron attenuation is observed on the left side of the coin cell as well as the right (as indicated in the Figure). The most pronounced detail in this radiograph is the ring of higher attenuation around the profile of the cell electrodes, which was first observed in Fig. 4c.

In situ radiography has revealed a noticeable trend in neutron attenuation throughout the overcharge test. No external failure of the cell was observed at any point throughout the test. Variations in neutron attenuation therefore can be attributed to mass transfer inside the cell due to electrochemical activity. It has been shown in the literature [31] that lithium concentration increases in the negative electrode upon charging and decreases in the cathode. It is therefore presumed that the graphite anode is at more risk for lithium deposition than the cathode.

The goal of this work is to relate the deposition of lithium on cell electrodes to the details shown in neutron radiograph images. A long-term objective is to utilize NR to detect and quantify the degree of deposition without the need for destructive analysis and direct observation. At this early stage in the work, however, destructive analysis was used to visually inspect the cell components to determine the cause of the increase in neutron attenuation during overcharge.

3.3 Comparison with destructive analysis

The results from in situ NR were validated by direct inspection of the cell. The cell used in this test was opened after neutron imaging was completed. The electrodes and other cell components were inspected both visually and with a digital microscope. The liquid electrolyte quickly evaporated upon opening of the cell case. The size of the cell electrodes compared to the battery case can be seen in Fig. 5b, which shows the anode of the cell from this study overlain on an identical, intact cell. It is clear that much of the change in neutron attenuation that was observed in Figs. 4 and 5a is located within the profile of the electrodes. The region of strong attenuation on the right side of the cell is located near the edge of the electrodes.

Fig. 5 **a** Processed radiograph image of NCA coin cell, 60 min into test; cell voltage = 4.8 V; **b** relative size and position of anode relative to cell case; **c** detail of solid deposition on anode surface immediately after cell case was opened; **d** overlay image showing processed radiograph data compared to anode profile

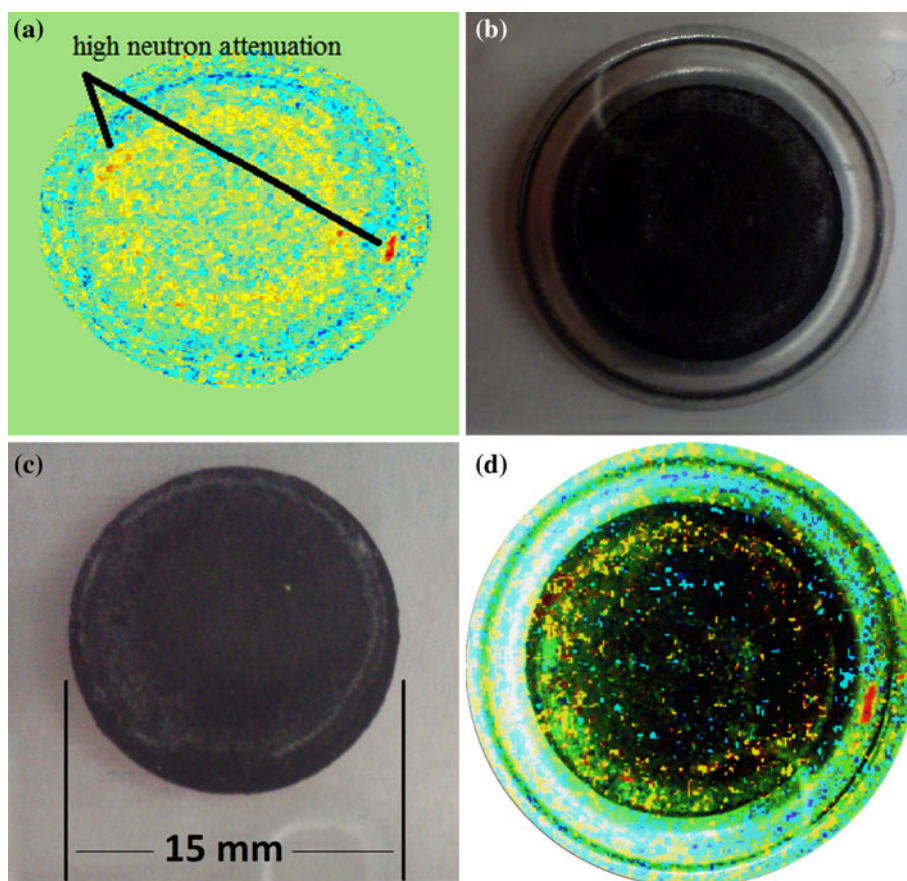
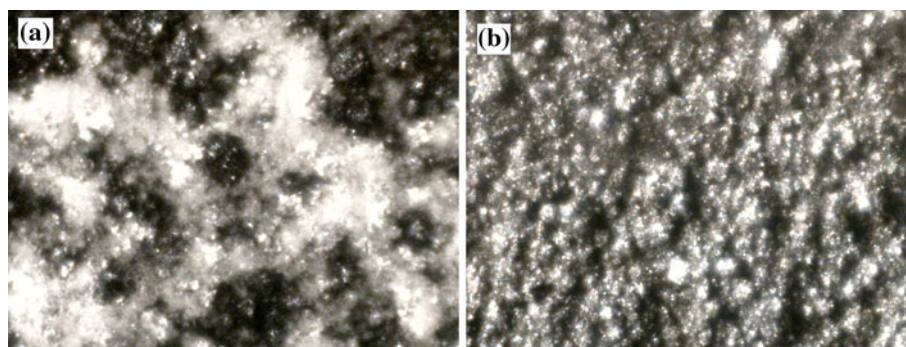


Fig. 6 Digital microscope image, $\times 20$ magnification: **a** portion of anode surface with visible solid deposit corresponding to high neutron attenuation; **b** portion of same anode surface with no visible solid deposit corresponding to low neutron attenuation



Visual inspection of the anode revealed a buildup of solid material on the surface of the graphite layer. There was no visible deposit on the cathode of the cell.

Figure 5c shows the anode as seen immediately after the cell case was opened. There is a silver-white-colored deposit on the surface of the anode, all around the edges of the circular electrode. Lithium buildup can be discerned from regular lithium-ion intercalation in graphite because lithiated graphite appears gold in color, whereas lithium itself is colored silver. The location of the lithium on the anode matches the pattern revealed by the in situ radiographs taken during the overcharge test. The image in Fig. 5d was generated by overlaying the processed radiograph in Fig. 5a with the photograph in Fig. 5c. This practice allowed direct comparison of the data in the radiograph with the visual inspection of the surface deposit on the electrode. It is clear from comparison of the images in Fig. 5 that the deposition of lithium on the surface of the anode was detected by NR.

A digital microscope was used to further examine the material observed on the anode. Figure 6a shows the anode surface at $20\times$ magnification in a region where the deposit was observed. For comparison, Fig. 6b shows a region of the anode, also at $20\times$ magnification, where the solid deposit was not observed. It is clear that the silver-colored material is deposited on the surface of the anode and does not alter the structure of the graphite. As mentioned earlier, deposition of solid material on the surface of an electrode is correlated with decreased electrochemical performance. The microscope images provide further justification that the observed buildup on the anode can be attributed to an abnormal deposit of material on overcharge, rather than a normal intercalation of ions into the graphite.

3.4 Comparison with mass spectrometry

The cell used in this experiment was analyzed using inductively coupled plasma mass spectrometry (ICP-MS). The UC Davis Interdisciplinary Center for Mass Spectrometry features an Agilent 7500 series mass spectrometer, supported by a New Wave Research UP-213 laser

ablation system. A portion of the solid deposit observed on the cell anode was transferred from the anode to a microscope slide; this enabled mass analysis of only the isolated solid deposit, as well as regions of the anode itself with and without the visible deposit. A total of 19 points on the slide and the anode were selected for ICP-MS analysis. Each point was $60\text{ }\mu\text{m}$ in diameter. Ablation was performed to a depth of $5\text{ }\mu\text{m}$ for a duration of 10 s per point. Element intensity counts were detected over a period of approximately 60 s including the ablation period. A washout delay of 90 s was used between MS points to purge the ablated particles from the enclosed environment of the ICP-MS.

The ICP-MS procedure generated a result file showing the counts of individual elements as a function of time throughout the ablation and subsequent detection period. Figure 7 displays the element intensity counts for the isolated solid deposit sample. The first 15 s worth of data are provided in the figure; intensity counts tended toward zero beyond that time period. Lithium (Li^7) is determined to be the most prevalent element in the deposit sample. The same plot is shown in Fig. 8 for a region of the graphite anode on

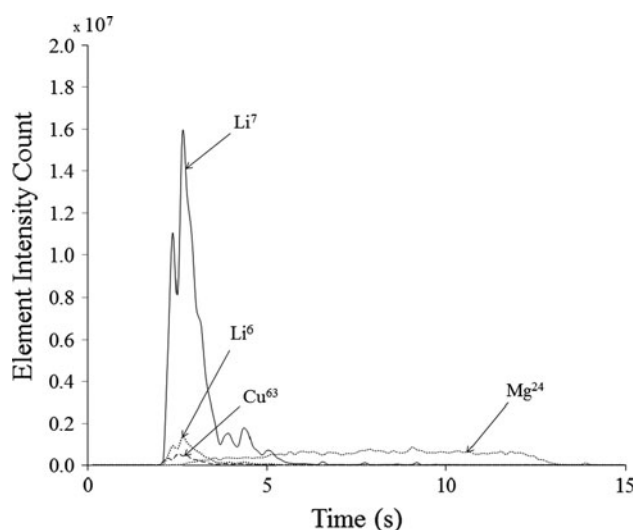


Fig. 7 ICP-MS element intensity count for sample of isolated solid deposit on glass slide

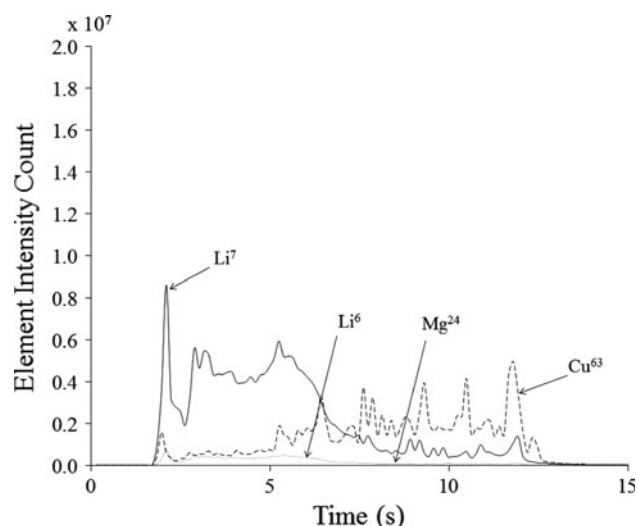


Fig. 8 ICP-MS element intensity count for region of graphite anode with no solid deposit

which no solid deposit was visible (i.e., near the outside of the anode profile). The presence of some lithium is expected as a result of the normal intercalation upon charging. However, it is clear that the intensity count of lithium is far lower for the deposit-free anode than for the deposited material itself.

4 Discussion and future work

The processed images generated with NR show the propagation of solid material on the anode of the battery. The overcharge condition in this study favored the removal of lithium from the electrochemical reaction and the formation of a solid material (such as lithium carbonate) on the anode surface. NR enabled detection of the accumulation of solid material within the battery cell, and visual inspection showed that a solid deposit had formed on the graphite anode of the cell. Element intensity counts generated with ICP-MS showed that this material is primarily composed of lithium. This result is of interest for the battery community because the removal of lithium from the normal intercalation reaction, and subsequent deposition of the lithium on the surface of cell electrodes, is detrimental to the performance and safety of the battery. We postulate that the solid material deposited on the anode surface is lithium carbonate (Li_2CO_3). Based on the work by Saito et al. [11], it is reasonable to believe that Li_2CO_3 forms on the electrode surface as a result of reaction of lithium metal with the electrolyte. Future work with neutron imaging of lithium-ion cells will examine this hypothesis.

The results of this study confirm the statement by Tang et al. [20] that lithium deposition preferentially occurs near

the edges of electrodes in a lithium-ion cell. This result justifies the need to construct a negative electrode with a larger profile than the positive electrode. This is significant for the design and packaging of battery cells for high-power applications where battery volume and material cost are significant constraints. The next steps in this work will seek to verify the relationship between lithium deposition and current density, as well as that between deposition and electrode profile overlap, as proposed by Tang et al. [20].

This study associates the anodic deposition of solid lithium compounds with overcharging of the cell. As suggested by Saito et al. [11], solid deposition may also occur on the positive electrode (cathode) during discharge. Further studies in this area will therefore involve applying in situ neutron imaging to more complex electrochemical cycles to examine the deposition of lithium throughout a realistic energy storage application. Another area of further work will be the development of a quantification technique to measure lithium deposition formation during electrochemical operation. The nondestructive character of NR along with the numerical nature of the data comprising the radiograph images will allow estimation of the quantity of material accumulating on the electrodes without the need to destroy the cell. The technique described in this study will be applied to cells operating under conditions that simulate the power demands of an electric-drive vehicle. Nondestructive, in situ visualization of cell electrodes will support the development of safe, reliable battery systems for advanced vehicles and other high-power applications.

5 Conclusions

Neutron radiography is demonstrated to be a useful technique for the study of overcharge conditions in lithium-ion batteries. A solid deposit composed primarily of lithium is formed on the surface of a graphite anode when the cell is charged to a high voltage. The experimental method described in this study allows visualization of lithium formation on a graphite electrode in an in situ fashion during an electrochemical test. Radiograph images are processed by applying neutron attenuation relationships to numerical bitmap data and isolating the change in the images compared to a pretest radiograph. Changes in neutron attenuation throughout the in situ test are attributed to the accumulation of solid material on electrodes. The locations of solid material deposition on the cell electrode shown by the radiographs are confirmed with direct visual observation and digital microscopy. Future work will expand on this technique to quantify lithium deposition in batteries for practical commercial and transportation applications.

Acknowledgments We are thankful for the support of Honghe Zheng at the Lawrence Berkeley National Laboratory. We also acknowledge the efforts of Ron Walker and the staff at the UC Davis McClellan Nuclear Research Center. This study was funded in part by the Fuel Cell, Hydrogen, and Hybrid Vehicle (FCH2V) Graduate Automotive Technology Education Center of Excellence at the University of California, Davis.

References

1. Tarascon J-M, Armand M (2001) *Nature* 415:359–367
2. Basu S (1999) *J Power Sources* 81–82:200–206
3. Selman J, Al Hallaj S, Uchida I, Hirano Y (2001) *J Power Sources* 97–98:726–732
4. Aksen J, Burke A, Kurani K (2008) Batteries for Plug-in Hybrid Electric Vehicles (PHEVs): goals and the state of technology circa 2008. Institute of Transportation Studies, University of California, Davis. UCD-ITS-RR-08-14
5. Aksen J, Kurani K, Burke A (2010) *Transp Policy* 17:173–182
6. Ohsaki T, Kishi T, Kuboki T, Takami N, Shimura N, Sato Y, Sekino M, Satohet A (2005) *J Power Sources* 146:97–100
7. Saito Y, Takano K, Negishi A (2001) *J Power Sources* 97–98:693–696
8. Spotnitz R, Franklin J (2003) *J Power Sources* 113:81–100
9. Huggins RA (2009) *Advanced batteries*. Springer Science, New York, pp 102–104
10. Tobishima S (1999) *J Power Sources* 81–82:882–886
11. Saito Y, Shikano M, Kobayashi H (2010) *J Power Sources*. doi: [10.1016/j.jpowsour.2010.12.098](https://doi.org/10.1016/j.jpowsour.2010.12.098)
12. Bhattacharyya R, Key B, Chen H, Best A, Hollenkamp A, Grey C (2010) *Nat Mater* 9(6):504–510
13. Chazalviel J (1990) *Phys Rev A* 42(12):7355–7367
14. Rosso M, Chazalviel J, Fleury V, Chassaing E (1994) *Electrochim Acta* 39(4):507–515
15. Brissot C, Rosso M, Chazalviel J, Lascaud S (1999) *J Power Sources* 81–82:925–929
16. Brissot C, Rosso M, Chazalviel J, Baudry P, Lascaud S (1998) *Electrochim Acta* 43:1569–1574
17. Arora P, Doyle M, White R (1999) *J Electrochem Soc* 146(10):3543–3553
18. Rosso M, Brissot C, Teyssot A, Dolle M, Sannier L, Tarascon J, Bouchet R, Lascaud S (2006) *Electrochim Acta* 51:5334–5340
19. Santhanagopalan S, Ramadass P, Zhang J (2009) *J Power Sources* 194:550–557
20. Tang M, Albertus P, Newman J (2009) *J Electrochem Soc* 156(5):A390–A399
21. Heller AK, Brenizer JS (2009) Neutron radiography. In: Anderson IS, et al (eds). *Neutron Imaging and Applications*. New York: Springer Science & Business Media, LLC
22. Heller A, Brenizer J (2009) In: McGreevy R, Bilheux H, Anderson I (eds) *Neutron imaging and applications: a reference for the imaging community*. Springer Science & Business Media, New York, p 72
23. de Beer F, Coetzer M, Fendeis D, Da Costa A, Silva E (2004) *Appl Radiat Isot* 61(4):609–616
24. Richards W, Gibbons M, Shields K (2004) *Appl Radiat Isotopes* 61:551–559
25. Kardjilov N, Hilger A, Mankea I, Strobl M, Treimer W, Banhart J (2005) *Nucl Instrum Methods Phys Res A* 542:16–21
26. Goers D, Holzapfel M, Scheifele W, Lehmann E, Vontobel P, Novák P (2004) *J Power Sources* 130:221–226
27. Lanz M, Lehmann E, Imhof R, Exnar I, Novák P (2001) *J Power Sources* 101:177–181
28. Kamata M, Esaka T, Kodama N, Fujini S, Yoneda K, Kanda K (1996) *J Electrochem Soc* 143(6):1866–1870
29. Kamata M, Esaka T, Kodama N, Fujini S, Yoneda K, Kanda K (1996) *Nucl Instrum Methods Phys Res A* 377:161–165
30. Tang H, Santamaria A, Kurniawan J, Park J, Yang T, Sohn Y (2010) *J Power Sources* 195:6774–6781
31. Siegel J, Liu X, Stefanopolou A, Hussey D, Jacobson D, Gorsich D (2011) *J Electrochem Soc* 158(5):A523–A529